Check for updates

ADVANCED MATERIALS
www.advmat.de

Ultrafast Sintering for Ceramic-Based All-Solid-State Lithium-Metal Batteries

*Shaojie Chen, Lu Nie, Xiangchen Hu, Yining Zhang, Yue Zhang, Yi Yu, and Wei Liu**

Long processing time and high temperatures are often required in sintering ceramic electrolytes, which lead to volatile element loss and high cost. Here, an ultrafast sintering method of microwave-induced carbothermal shock to fabricate various ceramic electrolytes in seconds is reported. Furthermore, it is also possible to integrate the electrode and electrolyte in one step by simultaneous co-sintering. Based on this ultrafast co-sintering technique, an all-solid-state lithium-metal battery with a high areal capacity is successfully achieved, realizing a promising electrochemical performance at room temperature. This method can extend to other various ceramic multilayer-based solid devices.

1. Introduction

All-solid-state metal batteries are attracting more and more attention as the next-generation energy storage system from both academia and industry, which is mainly due to their potential for good safety and high energy density.[1–5] Inorganic solid electrolytes are a significant part of all-solid-state lithium/sodium metal batteries, including NASICON-type,[6] perovskite-type,[7] garnet-type,[8,9] sulfide-based[10] Li superionic conductors and β-Al_2O_3,[11] NASICON-type,[12] and sulfide-based[13] Na superionic conductors. Among them, oxide ceramic electrolyte is one of the most promising solid electrolytes (SEs), owing to its high ionic conductivity, wide electrochemical window, and high chemical stability.[14–17] However, the densification of oxide ceramic electrolyte often requires a high temperature (>1100 °C) and a long holding time (>10 h) by conventional sintering, which is very likely to result in impurities, because of the significant risk of volatilization of Li/Na during high-temperature processing.[18–20] In addition, a stable and sufficient interfacial contact between SEs and electrodes could not be achieved by the conventional high-temperatures co-sintering method, due to severe element interdiffusion.[21] Therefore, the methods for the rapid densification of high-quality oxide ceramic electrolytes as well as the co-sintering of SEs and electrodes need to be developed as soon as possible.

Microwave sintering (MS) has been widely used for decades in the field of ceramic material processing.[22] Owing to the mechanism of directly transferring electromagnetic energy from microwave into heat, MS has several advantages, such as faster heating rate, shorter sintering time, higher energy efficiency, and enhanced materials properties, compared with conventional sintering.[23,24] It is reported that the improved densification effect with lower sintering temperature and shorter holding time for ceramics could be achieved by MS, which is due to the reduction in the sintering activation energy. The first attempt to fabricate $Li_7La_3Zr_2O_{12}$ (LLZO) ceramic electrolytes using microwave irradiation was carried out by Serena's group in 2015–2016. A relatively low ionic conductivity of around 10^{-9} S cm^{-1} was achieved through calcination (700 °C, 6 h) and annealing (1000 °C, 1 h) in a microwave furnace.[25] Besides, Gao et al. also prepared LLZO electrolytes and a relatively high ionic conductivity of 1.06×10^{-4} S cm^{-1} was revealed by MS at 1200 °C for 3 h.[26] However, the processing time is still too long to avoid the volatile Li element loss and mother powder is still needed to compensate for the loss. Recently, Hu's group reported an ultrafast high-temperature sintering (UHS) method to fabricate Ta-doped LLZO (LLZTO) garnet ceramic pellets in seconds through Joule-heating.[27] While, an inert atmosphere is needed.

In this work, we develop a microwave-assisted ultrafast sintering technique (MAUST) for various ceramic electrolytes by household microwave oven in air. With carbon black as microwave susceptor, the green bodies buried inside the carbon black matrix can be fully compacted within 25 s (**Figure 1**). Benefited from the ultrafast sintering process, the volatilization of Li/Na is effectively restrained. Besides, it is also able to achieve the ultrafast co-sintering of electrode–electrolyte integration. The obtained all-solid-state lithium-metal batteries (ASSLMBs) achieved good capacity due to compact electrode–electrolyte interface and restrained element interdiffusion. To replace the conventional sintering, this work presents an effective time and energy-saving pathway for the large-scale production of ceramic electrolytes and ASSLMBs.

2. Results and Discussion

Carbon materials are good absorbents of microwaves that can be rapidly heated by microwave radiation, which is called microwave-induced carbothermal shock.[28] In a typical ultrafast

S. Chen, L. Nie, X. Hu, Y. Zhang, Y. Zhang, Y. Yu, W. Liu
School of Physical Science and Technology
ShanghaiTech University
Shanghai 201210, China
E-mail: liuwei1@shanghaitech.edu.cn
Y. Yu, W. Liu
Shanghai Key Laboratory of High-resolution Electron Microscopy
ShanghaiTech University
Shanghai 201210, China
The ORCID identification number(s) for the author(s) of this article can be found under https://doi.org/10.1002/adma.202200430.

DOI: 10.1002/adma.202200430

 © 2022 Wiley-VCH GmbH

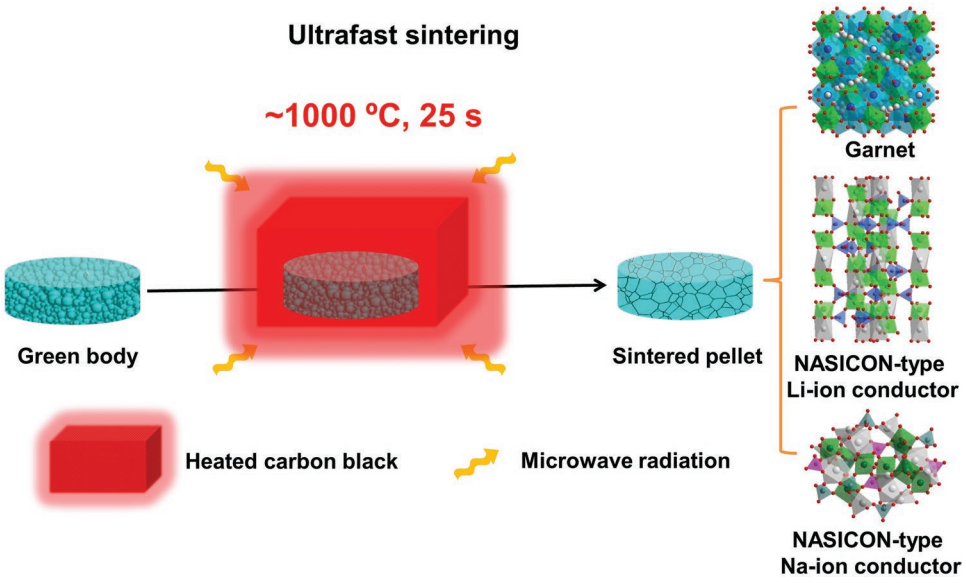

Figure 1. Schematic of the ultrafast sintering and co-sintering process. Through microwave-induced carbothermal shock, various ceramic electrolytes and electrode–electrolyte multilayers are ultrafast sintered in ≈25 s. The volatilization of Li/Na and the interdiffusion in electrode/electrolyte interface are effectively suppressed.

sintering process, a preheating process (500 W, ≈80 s) and a following sintering (800 W, ≈25 s) were included. The purpose of preheating process is to prevent the green body from cracking in a rapid heating process. Measured from the captured IR thermal image in the sintering step, the temperature is about 1000 °C (**Figure 2**A) and a whole IR thermal image capture procedure is provided in Video S1 in the Supporting Information. The rapid densification process in the sintering step was evidenced by the evolution of LLZTO pellet microstructure (Figure 2A, top). During the 25 s sintering time, LLZTO grains grew from ≈1.93 to ≈3.31 µm, and the microstructure of LLZTO pellet got much denser. The grain size statistics of each sample were presented in Figure S1 in the Supporting Information. As plotted in Figure 2B, the grain size and relative density had a synchronized raise trend with the sintering time. After 25 s, the MAUST-sintered LLZTO pellet achieved a high relative density of 94.5% ± 5.4%, which is higher than that of conventionally sintered LLZTO pellet (92.3% ± 5.8%). As shown in Figure S2 in the Supporting Information, the conventionally sintered LLZTO pellet had a looser microstructure than that of MAUST-sintered LLZTO pellets. Besides, if the sintering time was further prolonged to 30 s, the electrolyte pellet would melt into spherical shape and form plenty of pores inside the electrolyte, leading to a loose cross-sectional microstructure (Figure S3, Supporting Information). Importantly, the ultrashort sintering time can effectively restrain the volatilization of Li during high-temperature sintering process and thus the desired cubic garnet crystal structure could be obtained (Figure 2C). However, the LLZTO pellets sintered using conventional furnace have almost changed into $La_2Zr_2O_7$, indicating a very severe Li loss. Moreover, for the MAUST-sintered LLZTO and furnace-sintered LLZTO pellets, the amount of Li was determined by inductively coupled plasma optical emission spectrometry (ICP-OES). The Li retentions for MAUST-LLZTO and Furnace-LLZTO are 94% and 2% (Figure 2D and Table S1, Supporting Information), which is in agreement with the X-ray diffraction (XRD) results.

To further demonstrate the universality of ultrafast sintering technique, a NASICON-type Li-ion conductor $Li_{1.3}Al_{0.3}Ti_{1.7}(PO_4)_3$ (LATP) and a NASICON-type Na-ion conductor $Na_3Zr_2Si_2PO_{12}$ (NZSP) were also investigated. Similar with the LLZTO solid electrolyte, LATP and NZSP can also be rapidly densified by MAUST. The original crystal structure of ceramic electrolytes can be maintained (**Figure 3**A,C). Moreover, a dense microstructure of solid ceramic electrolyte can also be achieved (Figure 3B,D). As shown in Table S2 in the Supporting Information, the relative densities of MAUST-sintered LATP and MAUST-sintered NZSP pellets are 98.3% ± 3.4% and 95.6% ± 3.1%, respectively. And the relative densities of conventionally sintered LATP and conventionally sintered NZSP pellets are 96.7% ± 2.8% and 94.5% ± 2.5%, respectively. Compared with conventional sintering, MAUST shows better densification effect. The ionic conductivities of MAUST-LATP and MAUST-NZSP are 0.10 and 0.19 mS cm^{-1}, respectively (Figure S4, Supporting Information). Therefore, MAUST is a universal ultrafast sintering method to prepare various solid ceramic electrolytes.

Figure 3E is the comparison of MAUST with other sintering methods for various ceramic electrolytes, including garnet,[9,19,27,29–48] NASICON-type Li-ion conductor,[49–57] NASICON-type Na-ion conductor.[58–64] Compared to the traditional ceramic sintering technologies, including pressureless sintering, hot press sintering, spark plasma sintering (SPS), the sintering time has been greatly reduced, which is similar to the recently published UHS.[27] It is worth mentioning that the reduced process time is extremely important for Li/Na-ion conductors whose Li/Na element is volatile. For conventional sintering and thin-film processing, strategies need to be adopted to compensate the typical Li/Na loss during long time high-temperature sintering or low-temperature vacuum deposition.[45] Besides, the energy efficiency is very high due to

© 2022 Wiley-VCH GmbH

15214095, 2022, 33, Downloaded from https://onlinelibrary.wiley.com/doi/10.1002/adma.202200430 by Shanxi University, Wiley Online Library on [07/11/2024]. See the Terms and Conditions (https://onlinelibrary.wiley.com/terms-and-conditions) on Wiley Online Library for rules of use; OA articles are governed by the applicable Creative Commons License

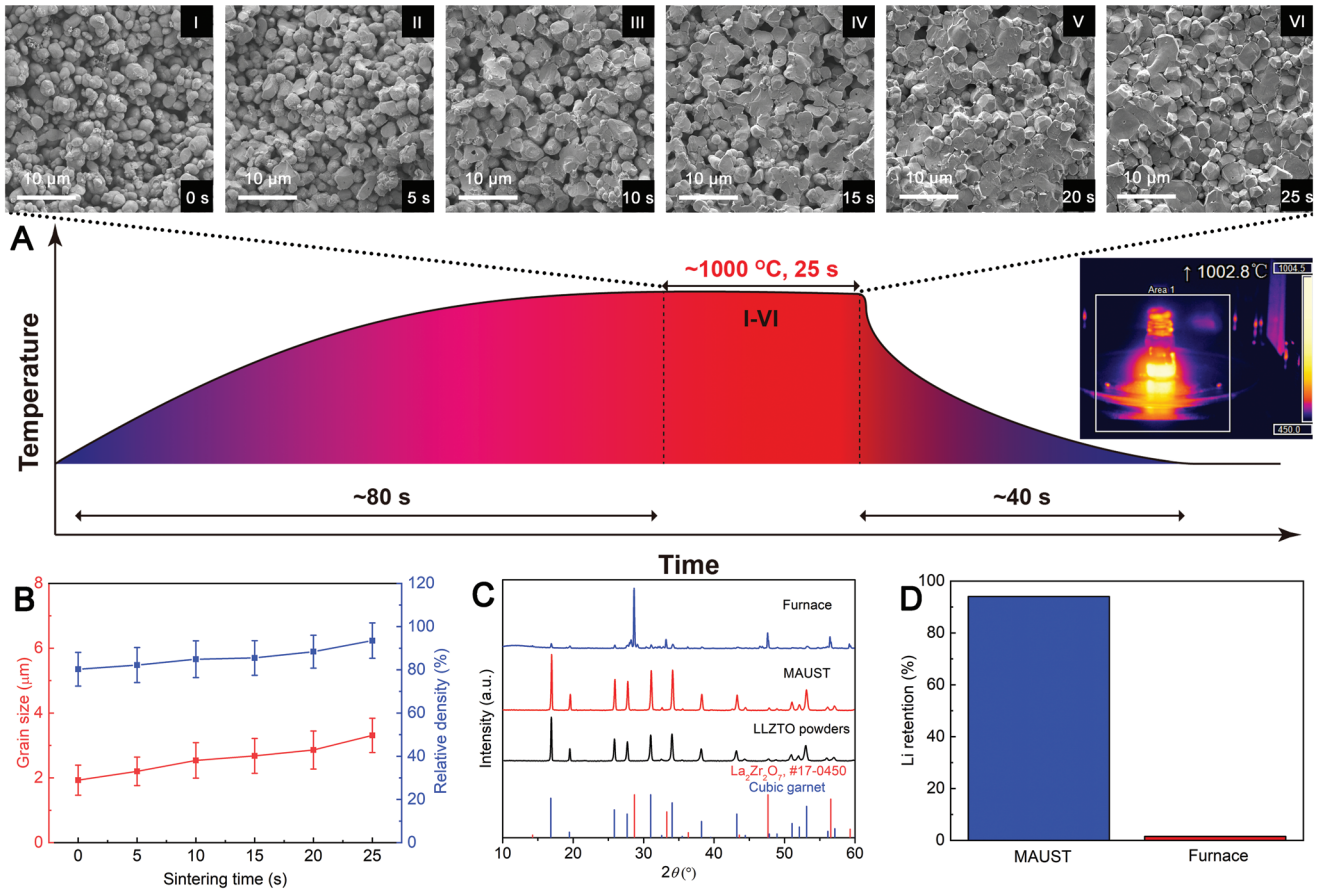

Figure 2. Ultrafast sintering of garnet ceramic electrolyte. A) Temperature curve of the ultrafast sintering process. The SEM images describe the morphology evolution of LLZTO ceramic during the 25 s sintering process. B) Relationship of grain size and relative density with sintering time. C) XRD patterns of the LLZTO powders, MAUST-sintered LLZTO, and furnace-sintered LLZTO ceramic pellets. D) Li retention of the MAUST-sintered and furnace-sintered LLZTO ceramic pellets.

the sintering mechanism of directly transfer electromagnetic energy to heat energy.

The ionic conductivities of LLZTO pellets were measured using gold as ion-blocking electrodes. As shown in **Figure 4**A, all the electrochemical impedance spectroscopy (EIS) curves are composed of a semicircle at medium frequency associated with the grain boundary response and an oblique line at low frequency corresponding to capacitive behavior of the gold electrodes.[65] Since the semicircle does not start from the origin, the real axis intercepts of semicircle at higher frequency and lower frequency represent the LLZTO bulk resistance and grain boundary resistance, respectively. For the MAUST–LLZTO pellet sintered for 25 s, the total ionic conductivity was about 0.60 mS cm^{-1} at room temperature, which is higher than the one sintered by conventional method of 0.30 mS cm^{-1} (Figure S5, Supporting Information). The fitting data can be found in Table S3 in the Supporting Information. In addition, with the increase of sintering time, the grain boundary impedances gradually decrease, which is consistent with the change of LLZTO pellet microstructure. Furthermore, the Arrhenius curves of these LLZTO pellets are presented in Figure 4B. Similar with the change trend of ionic conductivity, the activation energies got smaller along with sintering.

In order to determine the conductivity relaxation time, the Debye curves (Z'' vs log f) were plotted and fitted using a Lorentzian function (Figure 4C). The frequency of the peak maxima, a characteristic frequency of the ion conduction, can be given by the reciprocal of the conductivity relaxation time (τ) or conductivity (σ)[66,67]

$$2\pi f_{\max} = \omega = (\tau)^{-1} = \sigma(e_0 \varepsilon')^{-1} \quad (1)$$

where ε' (the real component of permittivity) is the frequency-independent permittivity and e_0 is the permittivity of free space (8.854×10^{-14} F cm^{-1}). It can be seen that the characteristic frequencies of LLZTO pellets with longer sintering time shifted toward higher frequency range, which is corresponding to a shorter relaxation time, indicating a faster ion conduction process.

The critical current density (CCD), at which the battery would short circuit, was measured by using a Li|MAUST-LLZTO|Li symmetric cell with a 20 μA cm^{-2} current density step and a 30 min duration (Figure 4D). The CCD was measured to be 0.46 mA cm^{-2}, which is better than the most values in the literatures, showing the LLZTO pellets prepared by MAUST have a great endurance for Li dendrites penetration. Moreover, the

© 2022 Wiley-VCH GmbH

15214095, 2022, 33, Downloaded from https://onlinelibrary.wiley.com/doi/10.1002/adma.202200430 by Shanxi University, Wiley Online Library on [07/11/2024]. See the Terms and Conditions (https://onlinelibrary.wiley.com/terms-and-conditions) on Wiley Online Library for rules of use; OA articles are governed by the applicable Creative Commons License

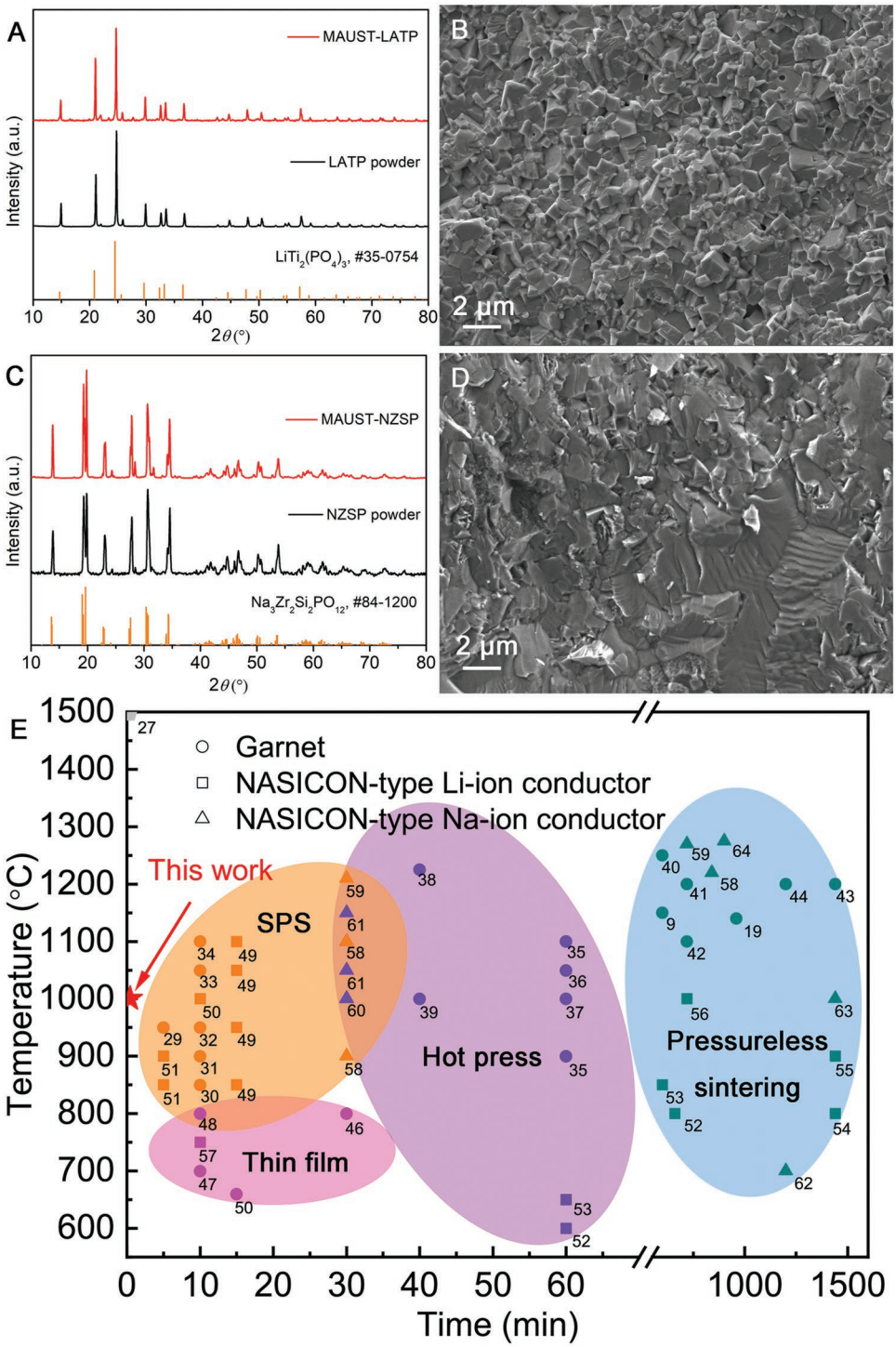

Figure 3. Universality of the MAUST and comparison with other sintering methods. A) XRD patterns of pristine LATP powder and MAUST-LATP pellet. B) SEM image of the microstructure of MAUST-LATP pellet. C) XRD patterns of pristine NZSP powder and MAUST-NZSP pellet. D) SEM image of the microstructure of MAUST-NZSP pellet. E) Comparison of various sintering technologies.

long-term cycling performance is shown in Figure 4E. At a current density of 0.1 mA cm^{-2}, the MAUST-LLZTO-based Li symmetric cell cycled for over 5000 h, indicating a good cycle stability.

Considering its high thermal stability, rapid lithium transport, and buffered volume expansion, a niobium tungsten oxide $Nb_{14}W_3O_{44}$ (NWO) was chosen as electrode material.[68,69] Due to the high-temperature process (≈1000 °C) of MAUST, electrode materials with high thermal stability are required. Therefore, some commonly used cathode materials were not adopted, such as $LiNi_{0.8}Co_{0.1}Mn_{0.1}O_2$ (NMC811), $LiCoO_2$ (LCO). As shown in Figures S6–S8 in the Supporting Information, the crystal structures of NMC811 and LCO have changed

© 2022 Wiley-VCH GmbH

15214095, 2022, 33, Downloaded from https://onlinelibrary.wiley.com/doi/10.1002/adma.202200430 by Shanxi University, Wiley Online Library on [07/11/2024]. See the Terms and Conditions (https://onlinelibrary.wiley.com/terms-and-conditions) on Wiley Online Library for rules of use; OA articles are governed by the applicable Creative Commons License

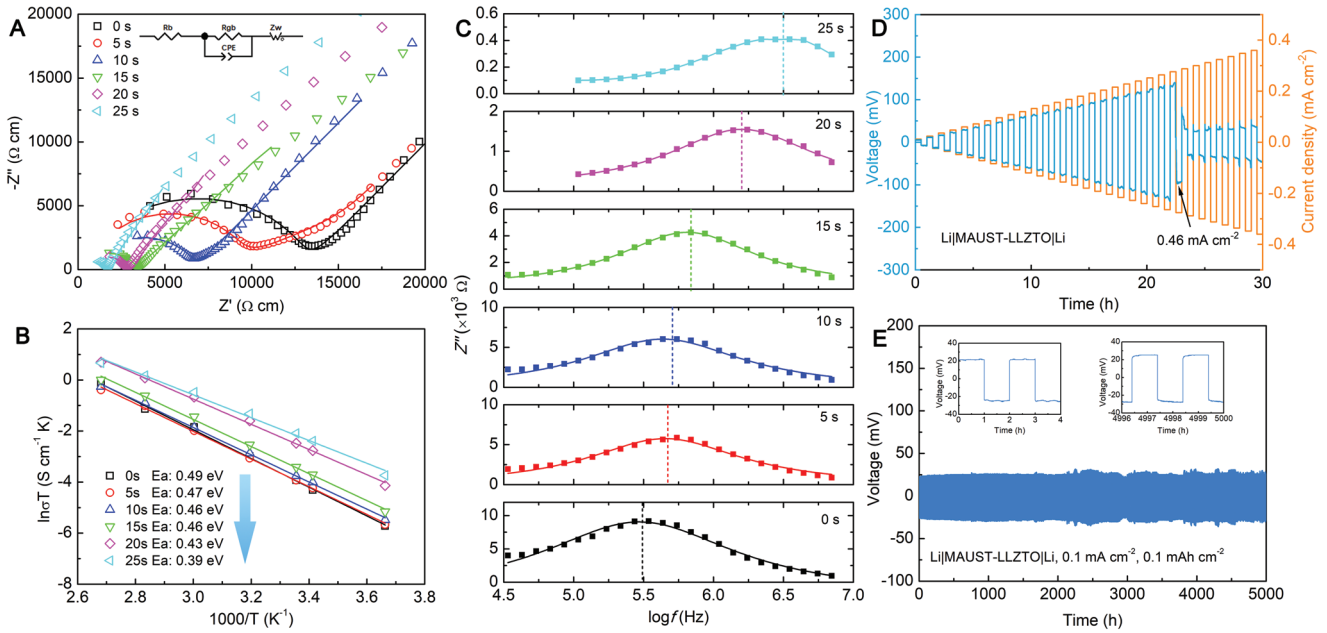

Figure 4. Electrochemical performances of ultrafast sintered garnet electrolyte. A) EIS curves of the garnet electrolyte pellets with different holding time. B) Corresponding Arrhenius plots for estimating the activation energies of Li-ion diffusion. C) Debye plots (imaginary impedance as a function of log*f*) and fitting curves of the garnet electrolyte pellets with different holding time. D) Voltage and current curves of the Li symmetric cell cycled under different current densities at room temperature. E) Long-term cycling performance of the Li symmetric cell at 0.1 mA cm^{-2}.

greatly after MAUST, while $Nb_{14}W_3O_{44}$ crystal structure can be maintained after MAUST. LATP and carbon black were chosen as electrolyte material and conductive additive, respectively. MAUST can simultaneously densify the integration of electrolyte layer and electrode layer in 25 s, resulting in a compact interface (**Figure 5**A,B). However, an obvious gap appeared at the electrode–electrolyte interface by conventional co-sintering (Figure S9, Supporting Information). In addition, as shown in Figure S10 in the Supporting Information, V_2O_5 and $LiFePO_4$ (LFP) electrode layers both exhibited a porous structure, which was due to that they melt during the microwave sintering and the porous structure appeared after sintering. Hence, we chose NWO as the electrode material in our study. As shown in Figure 5B, the energy-dispersive spectroscopy (EDS) mappings display that the P, Ti, and Al elements distribute throughout the electrode and electrolyte layers, because the LATP electrolyte was also added in electrode layer to provide efficient Li-ion transport. And the C, Nb, and W elements mainly distributed in the electrode layer, indicating that the MAUST can effectively avoid element cross-diffusion and guarantee good electronic conductivity by maintaining conductive carbon, because of the ultrafast sintering process. The conductive carbon black in the electrode would reduce the sintering density to a certain degree. However, the conductive carbon black has two important functions. First, the carbon black in the electrode could create enough "free space" to compensate the appearance of mechanical strains inside the composite electrode and to preserve the interfaces. Second, the conductive carbon black could ensure a good electron transport. Since LATP electrolyte reacts to lithium metal anode, a plastic crystal electrolyte (PCE) composed of succinonitrile and LiTFSI was used as buffer layer between LATP and Li anode. Owing to the compact interface and improved electronic conductivity, a relatively low total resistance was achieved (Figure S11, Supporting Information) and a thick electrode layer could be sufficiently utilized. The ASSLMBs achieved a high areal capacity of 2.09 mAh cm^{-2} (≈104.5 mAh g^{-1} in specific capacity) (Figure 5C) and a good cycling stability (Figure 5D) at room temperature (RT). The above electrochemical performance was much better than that of the conventional treated batteries (Figure S12, Supporting Information). To pursue higher energy density, the ASSLMBs with thick electrode (≈520 µm) and thin electrolyte (≈350 µm) were constructed (Figures S13 and S14, Supporting Information). Excitingly, a very high areal capacity of 5.7 mAh cm^{-2} was achieved at RT (Figure S15, Supporting Information), which is better than the most reported results (**Table 1**).

Last, the electrode/electrolyte interface of the ASSLMB was further investigated by focused ion beam-transmission electron microscopy (FIB-TEM), as shown in **Figure 6**A. Through MAUST, the electrode and electrolyte layers were integrated without any visible boundaries. And the Nb, W elements mainly distributed in the electrode layer region, indicating no element diffusion occurs (Figure 6B–F). Figure 6G shows the TEM image of electrolyte area. And the selected area electron diffraction (SAED) pattern is displayed in Figure 6H, which is consistent with LATP viewed along zone axis [010]. In addition, the high-resolution TEM (HRTEM) image is shown in Figure 6I. The interplanar spacings are 0.43 and 0.6 nm, which correspond to the (104) and ($\bar{1}$02) crystal planes of LATP, respectively. The similar TEM characterization for the electrode area also proved the $Nb_{14}W_3O_{44}$ cathode material was maintained after MAUST (Figure 6J–L), which agreed well with the XRD patterns before and after MAUST (Figure S6, Supporting Information).

© 2022 Wiley-VCH GmbH

15214095, 2022, 33, Downloaded from https://onlinelibrary.wiley.com/doi/10.1002/adma.202200430 by Shanxi University, Wiley Online Library on [07/11/2024]. See the Terms and Conditions (https://onlinelibrary.wiley.com/terms-and-conditions) on Wiley Online Library for rules of use; OA articles are governed by the applicable Creative Commons License

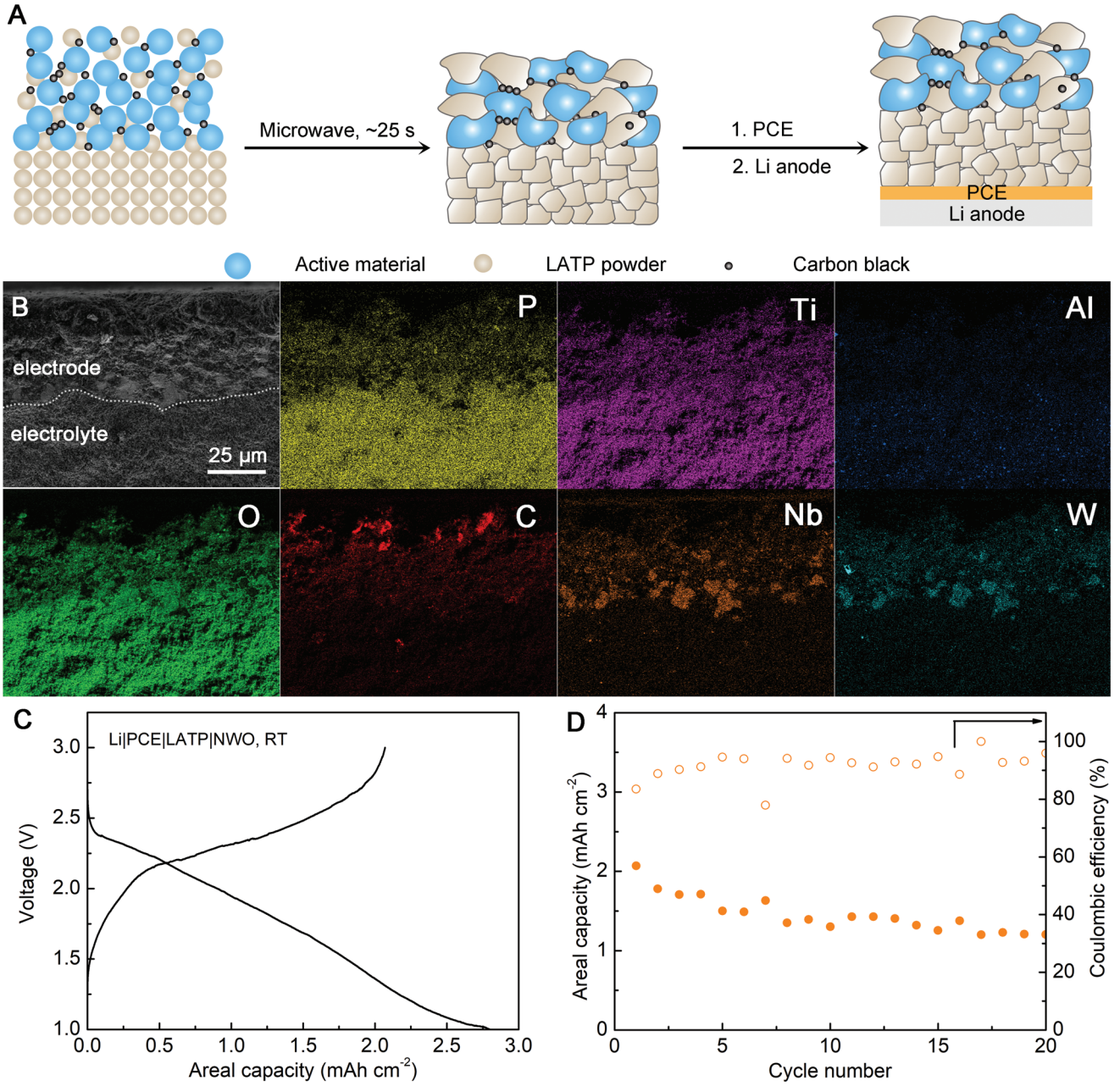

Figure 5. ASSLMBs enabled by ultrafast co-sintering. A) Schematic of the fabrication process of ASSLMBs. B) SEM image and corresponding EDS mapping of the interface of LATP and electrode layer. C) Charge–discharge profile of the ASSLMBs at 20 μA cm^{-2}. D) Corresponding cycling performance.

3. Conclusion

We have demonstrated an ultrafast sintering technique for various ceramic electrolytes and electrode–electrolyte multilayers enabled by microwave-induced carbothermal shock. Benefited from the ultrashort sintering time, volatile Li/Na loss and element cross-diffusion in electrode/electrolyte interface can be effectively suppressed. The as-constructed ASSLMBs using ultrafast co-sintering deliver a good electrochemical performance. In addition, besides the materials sintered in this work, MAUST might be applied to sintering other nonoxide materials, including metals, carbides, nitrides, borides, silicides, and so on. Furthermore, MAUST can sinter materials and devices with irregular structures, since the carbon black heater can conformally disperse around the structures. The present work provides an advanced material processing technique for the field of all-solid-state batteries and beyond.

4. Experimental Section

Preparation of LLZTO Powders: The $Li_{6.4}La_3Zr_{1.4}Ta_{0.6}O_{12}$ (LLZTO) powders were synthesized through a conventional solid-state reaction

© 2022 Wiley-VCH GmbH

15214095, 2022, 33, Downloaded from https://onlinelibrary.wiley.com/doi/10.1002/adma.202200430 by Shanxi University, Wiley Online Library on [07/11/2024]. See the Terms and Conditions (https://onlinelibrary.wiley.com/terms-and-conditions) on Wiley Online Library for rules of use; OA articles are governed by the applicable Creative Commons License

15214095, 2022, 33, Downloaded from https://onlinelibrary.wiley.com/doi/10.1002/adma.202200430 by Shanxi University, Wiley Online Library on [07/11/2024]. See the Terms and Conditions (https://onlinelibrary.wiley.com/terms-and-conditions) on Wiley Online Library for rules of use; OA articles are governed by the applicable Creative Commons License

Table 1. Literature overview of ASSLMBs based on Li-ion conducting ceramic electrolytes.

Battery structure	WorkingTemp [°C]	Current density	Areal capacity [mAh cm^{-2}]	Voltage [V vs Li/Li$^+$]	Cycling life	Method	Ref.
Li|LLZO|LTO[a)]	95	8.0 μA cm^{-2}	0.06	1.0–2.5	<20	Slurry coating	[70]
Li|LLZO|LFP[b)]	140	35.0 μA cm^{-2}	0.01	2.5–4.3	N/A[c)]	Aerosol deposition	[71]
Li|LLZO|NCM523[d)]	80	5.0 μA cm^{-2}	0.12	3.0–4.6	5	Two-step co-sintering[e)] (700 °C, 1 h)	[72]
Li|LLZO|NCM622[f)]	80	11.3 μA cm^{-2}	0.18	2.8–4.3	50	Two-step co-sintering (700 °C, 1 h)	[73]
Li|LLZO|LCO[g)]	100	5.8 μA cm^{-2}	0.11	3.0–4.05	40	Two-step co-sintering (700 °C, 1 h)	[21]
Li|LLZO|LCO	25	5.8 μA cm^{-2}	0.09	3.0–4.05	100	Two-step co-sintering (700 °C, 1 h)	[21]
Li|LLZO|LCO	25	10 μA cm^{-2}	0.15	3.0–4.05	5	Two-step co-sintering (700 °C, 1 h)	[74]
Li|LLZO|LCO	80	5.0 μA cm^{-2}	0.28	2.8–4.3	N/A	Two-step co-sintering (700 °C, 1 h)	[75]
Li|LLZO|LCO	RT	5.0 μA cm^{-2}	0.06	2.8–4.3	6	Two-step co-sintering (700 °C, 1 h)	[75]
Li|LLZO|V_2O_5	100	199.5 μA cm^{-2}	0.20	1.0–4.2	60	Two-step co-sintering (927 °C, 7 s)	[76]
Li|LLZO|LCO	25	3.5 μA cm^{-2}	0.03	2.5–4.2	100	PLD[h)]	[77]
Li|LLZO|LCO	RT	1.0 μA cm^{-2}	N/A	3.2–4.2	25	PLD	[78]
Li|SPE[i)]|LAGP[j)]|LFP	80	50.0 μA cm^{-2}	1.47	2.0–4.0	30	One-step co-sintering[k)] (650 °C, 1 h, 56 MPa)	[53]
Li|SPE|LATP|LCP[l)]	50	10.0 μA cm^{-2}	<0.01	3.5–5.0	N/A	PLD	[54]
Li|SPE|LATP|LFP	50	10.0 μA cm^{-2}	<0.01	2.8–4.1	N/A	PLD	[54]
Li|SPE|LATP|LCO	50	10.0 μA cm^{-2}	N/A	3.0–4.2	N/A	PLD	[79]
Li|PCE[m)]|LATP|NWO	RT	20.0 μA cm^{-2}	2.09	1.0–3.0	20	One-step co-sintering (1000 °C, 25 s)	This work
Li|PCE|LATP|NWO	RT	20.0 μA cm^{-2}	5.70	1.0–3.0	N/A	One-step co-sintering (1000 °C, 25 s)	This work

[a)]LTO, $Li_4Ti_5O_{12}$; [b)]LFP, $LiFePO_4$; [c)]N/A, not available; [d)]NCM523, $LiNi_{0.5}Co_{0.2}Mn_{0.3}O_2$; [e)]Two-step co-sintering, sinter electrolyte pellet first and then co-sinter electrode and electrolyte; [f)]NCM622, $LiNi_{0.6}Co_{0.2}Mn_{0.2}O_2$; [g)]LCO, $LiCoO_2$; [h)]PLD, pulse laser deposition; [i)]SPE, solid polymer electrolyte; [j)]LAGP, $Li_{1.5}Al_{0.5}Ge_{1.5}(PO_4)_3$; [k)]One-step co-sintering, sinter electrode and electrolyte multilayer in one step; [l)]LCP, $LiCoPO_4$; [m)]PCE, plastic crystal electrolyte.

method. $LiOH{\cdot}H_2O$ (≥98%, Aladdin), ZrO_2 (99.99%, Aladdin), La_2O_3 (99.99%, Macklin), and Ta_2O_5 (99.99%, Macklin) were stoichiometrically mixed by high speed ball-milling in isopropyl alcohol for 6 h. 20% excess of $LiOH{\cdot}H_2O$ was used to compensate the lithium volatilization during high-temperature calcination process. After being calcinated at 950 °C for 6 h, the LLZTO powders were finally obtained. LATP and NZSP powders were purchased from MTI Corporation.

Preparation of $Nb_{14}W_3O_{44}$ (NWO) Powders: $Nb_{14}W_3O_{44}$ was prepared by co-thermal oxidation of WO_3 (99.99%, Aladdin) and Nb_2O_5 (99.99%, Adamas). Required amounts of WO_3 and Nb_2O_5 were ground within an agate mortar, which were heated at 700 °C for 12 h and finally at 1200 °C for 12 h in air to obtain the $Nb_{14}W_3O_{44}$ powders.

Preparation of Various Ceramic Pellets by MAUST: The LLZTO, LATP, and NZSP ceramic powders were pressed into green bodies (diameter: 1.27 cm, thickness: 1 mm) under 200 MPa and directly used for MAUST. In a typical MAUST process, the green bodies buried in the center of a carbon black (CB, MTI Corporation) matrix with a weight of ≈1.5 g were first preheated under 500 W for ≈80 s, and then sintered at 800 W for ≈25 s with a household microwave oven (Midea, M1-230E) in air. Besides, a short time (≈40 s) was used to cool the sintered samples to room temperature and the cooling speed was ≈24 °C s^{-1}. The samples with different sintering times were prepared according to the same procedures except for the different sintering times. Before heating, the carbon black was compacted manually to ensure better heating effect. As shown in Figure S16 in the Supporting Information, the length, width, and height of microwave oven were 485, 393, and 293 mm, respectively. Besides, the microwave oven had a turning disk to ensure uniform heating. To avoid the flame and spark induced by carbon black, the MAUST process was carried out in an alumina crucible (diameter: 6.5 cm, volume: 150 mL) with a crucible cover.

Preparation of LLZTO Pellets using a Conventional Furnace: The as-prepared LLZTO powders with 2 wt% γ-Al_2O_3 (99.99%, Energy Chemical) powders as sintering additive were pressed into green bodies, and then sintered in a box furnace at 1100 °C for 12 h. To compensate the Li loss during the long time high-temperature sintering process, additional mother powders were paved around the green bodies. The control pellets for Li retention study were sintered at 1200 °C for 12 h in a furnace without using additional mother powder bed.

Co-Sintering of Electrode and Electrolyte Multilayers: The as-obtained $Nb_{14}W_3O_{44}$ electrode powders and LATP electrolyte powders were pressed into a double-layer green body with electrode layer and electrolyte layer. The electrode layer was consisted of $Nb_{14}W_3O_{44}$, LATP, and conductive carbon black (60:37:3 in wt%). The electrolyte layer only contained LATP powders, and the co-sintering procedure was the same as sintering of single ceramic electrolyte. For the co-sintering of electrode and electrolyte multilayers by conventional furnace, the sintering condition was 1000 °C for 1 h.

Materials Characterizations: Grain size distribution statistics of garnet electrolyte with various sintering times were carried out by using the Nano Measurer software. And for each sample, 50 grains were measured. The density was measured by Archimedes' method. A theoretical density of 5.5 g cm^{-3} was used to calculate the relative density of samples. XRD was performed on a Bruker D8 Advance using a Cu Kα radiation source. ICP-OES was conducted on an iCAP 7400 Radial. Scanning electron microscopy (SEM) images were recorded using a JEOL JSM-7800F. The cross-section of electrode–electrolyte interface was polished using ion-beam (JEOL, IB-19520CCP). TEM observation and EDS were conducted using a JEOL F200. The temperature of MAUST was measured by an infrared thermometer (Optris).

 © 2022 Wiley-VCH GmbH

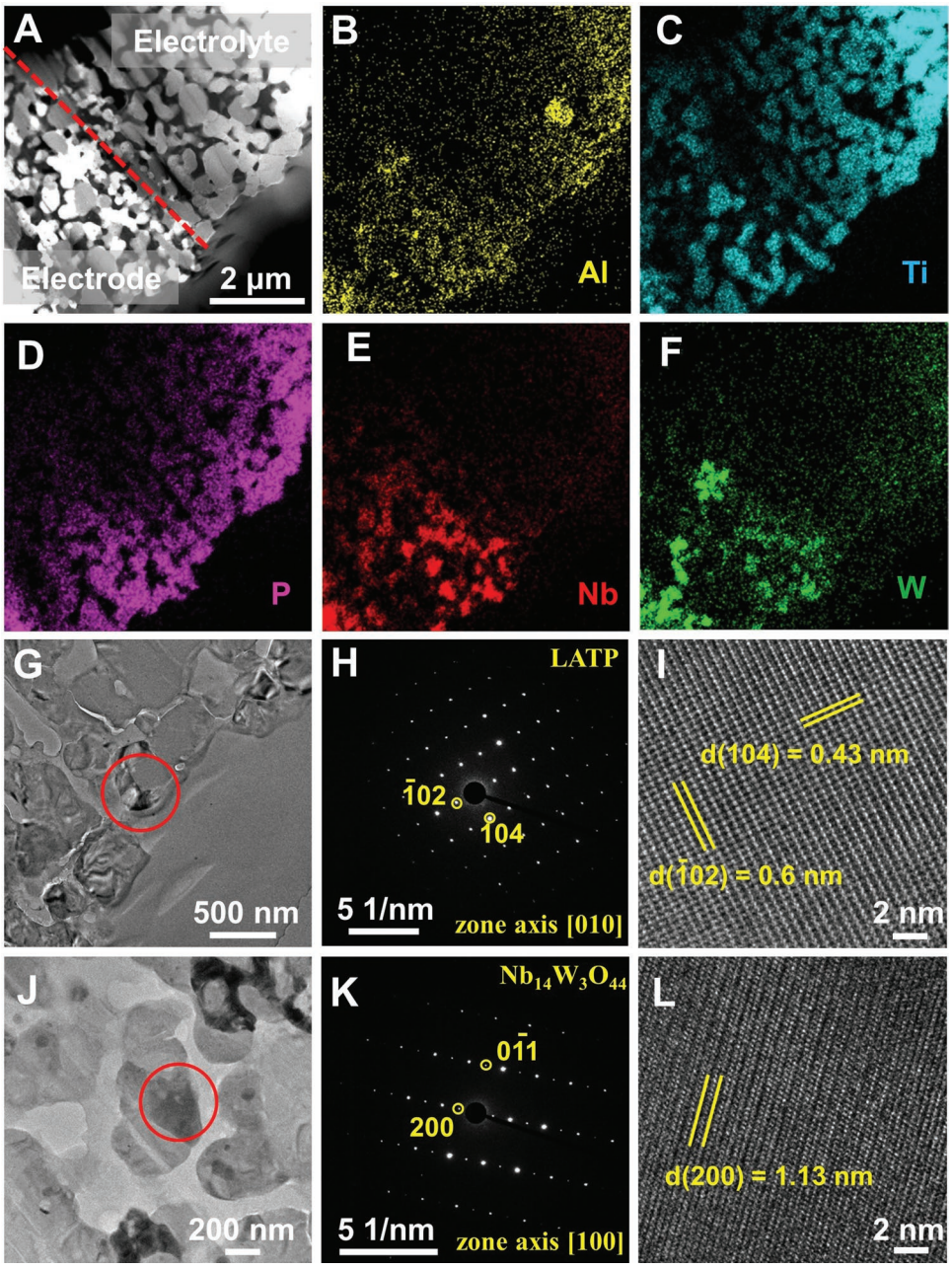

Figure 6. TEM characterization of ASSLMBs enabled by ultrafast co-sintering. A) TEM image of the electrode/electrolyte interface. B–F) Corresponding EDS mappings. G) TEM image of the electrolyte area. H) SAED pattern taken from the region within red circle in (G). I) Corresponding HRTEM image. J) TEM image of the electrode area. K) SAED pattern taken from the region within red circle in (J). L) Corresponding HRTEM image.

Electrochemical Tests: For measuring the ionic conductivity of various ceramic electrolytes, the blocking electrode was formed via sputtering gold for 5 min on the both sides of pellet. The EIS measurement was performed using a Biologic VMP300 potentiostat over a frequency range from 1 to 7 MHz. For a typical Li|MAUST-LLZTO|Li symmetric cell assembly, Li foil (Adamas-beta) was melted at ≈250 °C, and LLZTO pellet was directly placed into melted Li. After taking out the LLZTO pellet from melted Li and natural cooling down to room temperature, the Li symmetric cell was obtained. And the CCD value was determined under an initial current density of 0.02 mA cm^{-2} with an increasing step of 0.02 mA cm^{-2} at room temperature. The charge and discharge duration was set to be 30 min. The cells were also tested by galvanostatic cycling at 0.1 mA cm^{-2} and 0.1 mAh cm^{-2} with LAND system and Neware battery cycler. For the all-solid-state Li|PCE|LATP|NWO cells, the obtained NWO-LATP multilayer was used as electrode and electrolyte, respectively. Besides, an Au layer was sputtered as current collector and a PCE was added between LATP and Li to avoid the side reaction. The PCE was made by simply dissolving 5 mol% LiTFSI in succinonitrile (SN) at 60 °C. Besides, to stabilize the Li metal interface, 2 wt% $LiNO_3$ additives were added. Then, a piece of glass fiber (GF/C1822-047, Whatman) was used as host to soak PCE and was cooled down to room temperature to get a solid-state PCE film. The ASSLMBs were tested at a current density of 20 μA cm^{-2} and room temperature. The voltage range was 1.0–3.0 V.

© 2022 Wiley-VCH GmbH

15214095, 2022, 33, Downloaded from https://onlinelibrary.wiley.com/doi/10.1002/adma.202200430 by Shanxi University, Wiley Online Library on [07/11/2024]. See the Terms and Conditions (https://onlinelibrary.wiley.com/terms-and-conditions) on Wiley Online Library for rules of use; OA articles are governed by the applicable Creative Commons License

Supporting Information

Supporting Information is available from the Wiley Online Library or from the author.

Acknowledgements

S.C. and L.N. contributed equally to this work. This work was partially supported by National Key Research and Development Program (2019YFA0210600), National Natural Science Foundations of China (21805185, 21905174), and Shanghai Rising-Star Program (20QA1406600). CħEM, SPST of ShanghaiTech University (#EM02161943), and Shanghai Science and Technology Plan (21DZ2260400) are also acknowledged for supporting.

Conflict of Interest

The authors declare no conflict of interest.

Data Availability Statement

The data that support the findings of this study are available from the corresponding author upon reasonable request.

Keywords

all-solid-state lithium batteries, electrode–electrolyte interfaces, high areal capacity, solid electrolytes, ultrafast sintering

Received: January 14, 2022
Revised: May 25, 2022
Published online: July 13, 2022

[1] A. Manthiram, X. Yu, S. Wang, *Nat. Rev. Mater.* **2017**, *2*, 16103.
[2] C. Yang, Q. Wu, W. Xie, X. Zhang, A. Brozena, J. Zheng, M. N. Garaga, B. H. Ko, Y. Mao, S. He, Y. Gao, P. Wang, M. Tyagi, F. Jiao, R. Briber, P. Albertus, C. Wang, S. Greenbaum, Y. Y. Hu, A. Isogai, M. Winter, K. Xu, Y. Qi, L. Hu, *Nature* **2021**, *598*, 590.
[3] X. Chi, M. Li, J. Di, P. Bai, L. Song, X. Wang, F. Li, S. Liang, J. Xu, J. Yu, *Nature* **2021**, *592*, 551.
[4] Y. Pang, J. Pan, J. Yang, S. Zheng, C. Wang, *Electrochem. Energy Rev.* **2021**, *4*, 169.
[5] W. Zhao, J. Yi, P. He, H. Zhou, *Electrochem. Energy Rev.* **2019**, *2*, 574.
[6] S. D. Jackman, R. A. Cutler, *J. Power Sources* **2012**, *218*, 65.
[7] Z. Jiang, S. Wang, X. Chen, W. Yang, X. Yao, X. Hu, Q. Han, H. Wang, *Adv. Mater.* **2020**, *32*, 1906221.
[8] H. Huo, J. Liang, N. Zhao, X. Li, X. Lin, Y. Zhao, K. Adair, R. Li, X. Guo, X. Sun, *ACS Energy Lett.* **2020**, *5*, 2156.
[9] Y. Shao, H. Wang, Z. Gong, D. Wang, B. Zheng, J. Zhu, Y. Lu, Y.-S. Hu, X. Guo, H. Li, X. Huang, Y. Yang, C.-W. Nan, L. Chen, *ACS Energy Lett.* **2018**, *3*, 1212.
[10] L. Ye, X. Li, *Nature* **2021**, *593*, 218.
[11] G. Chen, J. Lu, X. Zhou, L. Chen, X. Jiang, *Ceram. Int.* **2016**, *42*, 16055.
[12] C. Wang, J. Gao, X. Gao, Y. Zhao, *Cell Rep. Phys. Sci.* **2021**, *2*, 100478.
[13] H. Jia, Y. Sun, Z. Zhang, L. Peng, T. An, J. Xie, *Energy Storage Mater.* **2019**, *23*, 508.
[14] J. Dai, C. Yang, C. Wang, G. Pastel, L. Hu, *Adv. Mater.* **2018**, *30*, 1802068.
[15] T. Famprikis, P. Canepa, J. A. Dawson, M. S. Islam, C. Masquelier, *Nat. Mater.* **2019**, *18*, 1278.
[16] N. Zhao, W. Khokhar, Z. Bi, C. Shi, X. Guo, L.-Z. Fan, C.-W. Nan, *Joule* **2019**, *3*, 1190.
[17] S. Chen, J. Zhang, L. Nie, X. Hu, Y. Huang, Y. Yu, W. Liu, *Adv. Mater.* **2020**, *33*, 2002325.
[18] S. Chen, X. Hu, W. Bao, Z. Wang, Q. Yang, L. Nie, X. Zhang, J. Zhang, Y. Jiang, Y. Han, C. Wan, J. Xie, Y. Yu, W. Liu, *Cell Rep. Phys. Sci.* **2021**, *2*, 100569.
[19] Y. Li, J.-T. Han, C.-A. Wang, H. Xie, J. B. Goodenough, *J. Mater. Chem.* **2012**, *22*, 15357.
[20] R. Wei, S. Chen, T. Gao, W. Liu, *Nano Sel.* **2021**, *2*, 2256.
[21] F. Han, J. Yue, C. Chen, N. Zhao, X. Fan, Z. Ma, T. Gao, F. Wang, X. Guo, C. Wang, *Joule* **2018**, *2*, 497.
[22] V. G. Karayannis, *IOP Conf. Ser.: Mater. Sci. Eng.* **2016**, *161*, 012068.
[23] H. J. Kitchen, S. R. Vallance, J. L. Kennedy, N. Tapia-Ruiz, L. Carassiti, A. Harrison, A. G. Whittaker, T. D. Drysdale, S. W. Kingman, D. H. Gregory, *Chem. Rev.* **2014**, *114*, 1170.
[24] R. Jiang, Y. Da, X. Han, Y. Chen, Y. Deng, W. Hu, *Cell Rep. Phys. Sci.* **2021**, *2*, 100302.
[25] M. Amores, T. E. Ashton, P. J. Baker, E. J. Cussen, S. A. Corr, *J. Mater. Chem. A* **2016**, *4*, 1729.
[26] D. Gao, R. Wu, P. Chen, T. Hong, J. Cheng, *Mater. Res. Express* **2020**, *6*, 125539.
[27] C. Wang, W. Ping, Q. Bai, H. Cui, R. Hensleigh, R. Wang, A. H. Brozena, Z. Xu, J. Dai, Y. Pei, C. Zheng, G. Pastel, J. Gao, X. Wang, H. Wang, J. C. Zhao, B. Yang, X. R. Zheng, J. Luo, Y. Mo, B. Dunn, L. Hu, *Science* **2020**, *368*, 521.
[28] G. Zhong, S. Xu, Q. Dong, X. Wang, L. Hu, *Adv. Funct. Mater.* **2021**, *31*, 2010968.
[29] C. Li, Y. Liu, J. He, K. S. Brinkman, *J. Alloys Compd.* **2017**, *695*, 3744.
[30] S.-W. Baek, J.-M. Lee, T. Y. Kim, M.-S. Song, Y. Park, *J. Power Sources* **2014**, *249*, 197.
[31] M. M. Ahmad, *Ceram. Int.* **2015**, *41*, 6398.
[32] M. Botros, R. Djenadic, O. Clemens, M. Möller, H. Hahn, *J. Power Sources* **2016**, *309*, 108.
[33] M. Kotobuki, S. Song, R. Takahashi, S. Yanagiya, L. Lu, *J. Power Sources* **2017**, *349*, 105.
[34] M. Kotobuki, M. Koishi, *J. Alloys Compd.* **2020**, *826*, 154213.
[35] I. N. David, T. Thompson, J. Wolfenstine, J. L. Allen, J. Sakamoto, B. Viyas, *J. Am. Ceram. Soc.* **2015**, *98*, 1209.
[36] J. Wolfenstine, E. Rangasamy, J. L. Allen, J. Sakamoto, *J. Power Sources* **2012**, *208*, 193.
[37] E. Rangasamy, J. Wolfenstine, J. Sakamoto, *Solid State Ionics* **2012**, *206*, 28.
[38] M. Sato, R. Garcia-Mendez, J. Sakamoto, *J. Asian Ceram. Soc.* **2020**, *8*, 793.
[39] G. Han, B. Kinzer, R. Garcia-Mendez, H. Choe, J. Wolfenstine, J. Sakamoto, *J. Eur. Ceram. Soc.* **2020**, *40*, 1999.
[40] X. Huang, C. Liu, Y. Lu, T. Xiu, J. Jin, M. E. Badding, Z. Wen, *J. Power Sources* **2018**, *382*, 190.
[41] G. V. Alexander, N. C. Rosero-Navarro, A. Miura, K. Tadanaga, R. Murugan, *J. Mater. Chem. A* **2018**, *6*, 21018.
[42] Y. Wang, P. Yan, J. Xiao, X. Lu, J.-G. Zhang, V. L. Sprenkle, *Solid State Ionics* **2016**, *294*, 108.
[43] W. Xia, B. Xu, H. Duan, Y. Guo, H. Kang, H. Li, H. Liu, *ACS Appl. Mater. Interfaces* **2016**, *8*, 5335.
[44] G. V. Alexander, S. Patra, S. V. Sobhan Raj, M. K. Sugumar, M. M. Ud Din, R. Murugan, *J. Power Sources* **2018**, *396*, 764.
[45] R. Pfenninger, M. Struzik, I. Garbayo, E. Stilp, J. L. M. Rupp, *Nat. Energy* **2019**, *4*, 475.
[46] J. Tan, A. Tiwari, *ECS Solid State Lett.* **2012**, *1*, Q57.

© 2022 Wiley-VCH GmbH

15214095, 2022, 33, Downloaded from https://onlinelibrary.wiley.com/doi/10.1002/adma.202200430 by Shanxi University, Wiley Online Library on [07/11/2024]. See the Terms and Conditions (https://onlinelibrary.wiley.com/terms-and-conditions) on Wiley Online Library for rules of use; OA articles are governed by the applicable Creative Commons License

[47] R.-J. Chen, M. Huang, W.-Z. Huang, Y. Shen, Y.-H. Lin, C.-W. Nan, *J. Mater. Chem. A* **2014**, *2*, 13277.
[48] M. Bitzer, T. Van Gestel, S. Uhlenbruck, B. H. Peter, *Thin Solid Films* **2016**, *615*, 128.
[49] E. C. Bucharsky, K. G. Schell, A. Hintennach, M. J. Hoffmann, *Solid State Ionics* **2015**, *274*, 77.
[50] M. Kotobuki, S. Yanagiya, *J. Alloys Compd.* **2021**, *862*, 158641.
[51] K. Waetzig, A. Rost, C. Heubner, M. Coeler, K. Nikolowski, M. Wolter, J. Schilm, *J. Alloys Compd.* **2020**, *818*, 153237.
[52] Y. Zhu, T. Wu, J. Sun, M. Kotobuki, *Solid State Ionics* **2020**, *350*, 115320.
[53] A. Paolella, W. Zhu, G. Bertoni, A. Perea, H. Demers, S. Savoie, G. Girard, N. Delaporte, A. Guerfi, M. Rumpel, H. Lorrmann, G. P. Demopoulos, K. Zaghib, *Adv. Mater. Interfaces* **2020**, *7*, 2070069.
[54] J. Xie, N. Imanishi, T. Zhang, A. Hirano, Y. Takeda, O. Yamamoto, *J. Power Sources* **2009**, *192*, 689.
[55] T. Yoshinari, R. Koerver, P. Hofmann, Y. Uchimoto, W. G. Zeier, J. Janek, *ACS Appl. Mater. Interfaces* **2019**, *11*, 23244.
[56] M. Pérez-Estébanez, J. Isasi-Marín, A. Rivera-Calzada, C. León, M. Nygren, *J. Alloys Compd.* **2015**, *651*, 636.
[57] X. M. Wu, S. Chen, F. R. Mai, J. H. Zhao, Z. Q. He, *Ionics* **2012**, *19*, 589.
[58] J. S. Lee, C. M. Chang, Y. I. Lee, J. H. Lee, S. H. Hong, *J. Am. Ceram. Soc.* **2004**, *87*, 305.
[59] H. Wang, K. Okubo, M. Inada, G. Hasegawa, N. Enomoto, K. Hayashi, *Solid State Ionics* **2018**, *322*, 54.
[60] D. Zhu, F. Luo, Z. Xie, W. Zhou, *Rare Met.* **2006**, *25*, 39.
[61] D. M. Zhu, Z. L. Xie, F. Luo, W. C. Zhou, *Key Eng. Mater.* **2007**, *334–335*, 149.
[62] K. Suzuki, K. Noi, A. Hayashi, M. Tatsumisago, *Scr. Mater.* **2018**, *145*, 67.
[63] O. Tillement, J. C. Couturier, J. Angenault, M. Quarton, *Solid State Ionics* **1991**, *48*, 249.
[64] K. Hayashi, K. Shima, F. Sugiyama, *J. Electrochem. Soc.* **2013**, *160*, A1467.
[65] K. K. Fu, Y. Gong, B. Liu, Y. Zhu, S. Xu, Y. Yao, W. Luo, C. Wang, S. D. Lacey, J. Dai, Y. Chen, Y. Mo, E. Wachsman, L. Hu, *Sci. Adv.* **2017**, *3*, e1601659.
[66] W. Liu, S. W. Lee, D. Lin, F. Shi, S. Wang, A. D. Sendek, Y. Cui, *Nat. Energy* **2017**, *2*, 17035.
[67] U. Dash, S. Sahoo, S. K. S. Parashar, P. Chaudhuri, *J. Adv. Ceram.* **2014**, *3*, 98.
[68] Y. Yang, H. Zhu, J. Xiao, H. Geng, Y. Zhang, J. Zhao, G. Li, X. L. Wang, C. C. Li, Q. Liu, *Adv. Mater.* **2020**, *32*, 1905295.
[69] K. J. Griffith, K. M. Wiaderek, G. Cibin, L. E. Marbella, C. P. Grey, *Nature* **2018**, *559*, 556.
[70] J. van den Broek, S. Afyon, J. L. M. Rupp, *Adv. Energy Mater.* **2016**, *6*, 1600736.
[71] C.-W. Ahn, J.-J. Choi, J. Ryu, B.-D. Hahn, J.-W. Kim, W.-H. Yoon, J.-H. Choi, J.-S. Lee, D.-S. Park, *J. Power Sources* **2014**, *272*, 554.
[72] T. Liu, Y. Zhang, X. Zhang, L. Wang, S.-X. Zhao, Y.-H. Lin, Y. Shen, J. Luo, L. Li, C.-W. Nan, *J. Mater. Chem. A* **2018**, *6*, 4649.
[73] X. Guo, L. Hao, Y. Yang, Y. Wang, Y. Lu, H. Yu, *J. Mater. Chem. A* **2019**, *7*, 25915.
[74] S. Ohta, S. Komagata, J. Seki, T. Saeki, S. Morishita, T. Asaoka, *J. Power Sources* **2013**, *238*, 53.
[75] T. Liu, Y. Ren, Y. Shen, S.-X. Zhao, Y. Lin, C.-W. Nan, *J. Power Sources* **2016**, *324*, 349.
[76] G. Zhong, C. Wang, R. Wang, W. Ping, S. Xu, H. Qiao, M. Cui, X. Wang, Y. Zhou, D. J. Kline, M. R. Zachariah, L. Hu, *Energy Storage Mater.* **2020**, *30*, 385.
[77] S. Ohta, T. Kobayashi, J. Seki, T. Asaoka, *J. Power Sources* **2012**, *202*, 332.
[78] T. Kato, T. Hamanaka, K. Yamamoto, T. Hirayama, F. Sagane, M. Motoyama, Y. Iriyama, *J. Power Sources* **2014**, *260*, 292.
[79] J. Xie, N. Imanishi, T. Zhang, A. Hirano, Y. Takeda, O. Yamamoto, *J. Power Sources* **2009**, *189*, 365.

© 2022 Wiley-VCH GmbH

15214095, 2022, 33, Downloaded from https://onlinelibrary.wiley.com/doi/10.1002/adma.202200430 by Shanxi University, Wiley Online Library on [07/11/2024]. See the Terms and Conditions (https://onlinelibrary.wiley.com/terms-and-conditions) on Wiley Online Library for rules of use; OA articles are governed by the applicable Creative Commons License